

1 **Title: The spatial structure of the tumor immune microenvironment can**  
2 **explain and predict patient response in high-grade serous carcinoma**

3  
4 **Authors:** Lucy Van Kleunen\*<sup>1</sup>, Mansooreh Ahmadian<sup>2</sup>, Miriam D Post<sup>3</sup>, Rebecca J Wolsky<sup>3</sup>,  
5 Christian Rickert<sup>4</sup>, Kimberly Jordan<sup>4</sup>, Junxiao Hu<sup>5</sup>, Jennifer K. Richer<sup>3</sup>, Nicole A. Marjon<sup>6</sup>, Kian  
6 Behbakht<sup>6</sup>, Matthew J. Sikora<sup>3</sup>, Benjamin G. Bitler<sup>6</sup>, Aaron Clauset\*<sup>1,7,8</sup>

7  
8 **Running Title: Spatial structure of the tumor microenvironment in HGSC**

9  
10 **Affiliations:**

11 <sup>1</sup>Department of Computer Science, University of Colorado, Boulder, USA

12 <sup>2</sup>Department of Biostatistics and Informatics, Colorado School of Public Health, University of  
13 Colorado Anschutz Medical Campus, Aurora, CO, USA

14 <sup>3</sup>Department of Pathology, The University of Colorado Anschutz Medical Campus

15 <sup>4</sup>Department of Immunology and Microbiology, The University of Colorado Anschutz Medical  
16 Campus

17 <sup>5</sup>Department of Pediatrics, Cancer Center Biostatistics Core, University of Colorado Anschutz  
18 Medical Campus, CO, USA

19 <sup>6</sup>Department of OB/GYN, The University of Colorado Anschutz Medical Campus

20 <sup>7</sup>BioFrontiers Institute, University of Colorado, Boulder, CO, USA

21 <sup>8</sup>Santa Fe Institute, Santa Fe, NM, USA

22  
23 \*Corresponding authors:

24  
25 Lucy Van Kleunen

26 [lucy.vankleunen@colorado.edu](mailto:lucy.vankleunen@colorado.edu)

27  
28 Aaron Clauset

29 [aaron.clauset@colorado.edu](mailto:aaron.clauset@colorado.edu)

30  
31 **Conflict of Interest:** The authors declare no potential conflicts of interest.

32 **Abstract:**

33

34 Despite ovarian cancer being the deadliest gynecological malignancy, there has been little

35 change to therapeutic options and mortality rates over the last three decades. Recent studies

36 indicate that the composition of the tumor immune microenvironment (TIME) influences patient

37 outcomes but are limited by a lack of spatial understanding. We performed multiplexed ion beam

38 imaging (MIBI) on 83 human high-grade serous carcinoma tumors — one of the largest protein-

39 based, spatially-intact, single-cell resolution tumor datasets assembled — and used statistical and

40 machine learning approaches to connect features of the TIME spatial organization to patient

41 outcomes. Along with traditional clinical/immunohistochemical attributes and indicators of

42 TIME composition, we found that several features of TIME spatial organization had significant

43 univariate correlations and/or high relative importance in high-dimensional predictive models.

44 The top performing predictive model for patient progression-free survival (PFS) used a

45 combination of TIME composition and spatial features. Results demonstrate the importance of

46 spatial structure in understanding how the TIME contributes to treatment outcomes.

47 Furthermore, the present study provides a generalizable roadmap for spatial analyses of the

48 TIME in ovarian cancer research.

49 **Main Text:**

50 **INTRODUCTION**

51 High grade serous carcinoma (HGSC) of the ovary, fallopian tube, and peritoneum is the  
52 gynecologic malignancy with the highest mortality rate (1,2). Over the last three decades there  
53 has been little improvement in the survival rate for patients diagnosed with HGSC, due in part to  
54 limited therapeutic options beyond chemotherapy, poor early detection rates, and a limited  
55 understanding of both the pathogenesis and the role of the tumor microenvironment. To further  
56 understand the drivers of HGSC and therapy response, several studies have examined patients  
57 who are disease-free 10 years after initial treatment (3). Long-term survival has been partially  
58 attributed to an enhanced anti-tumor immune response (4,5), indicating a clinical need to further  
59 define the tumor immune microenvironment (TIME) and elucidate its influence on patient  
60 outcomes.

61 Although HGSC often has a high degree of immune infiltrates, including macrophages  
62 that can compose up to 50% of all immune cells in the TIME (6), immune therapies have had  
63 limited impact on improving outcomes for individuals with HGSC (7). Prior studies of the  
64 HGSC TIME have discovered that selective immune cell infiltration often correlates with  
65 improved patient outcomes. Specifically, infiltration of CD3+ T cells and CD19+ B cells is  
66 associated with an average 62-month and 6-month survival benefit, respectively (8,9). In  
67 contrast, an increased density of CD163+ tumor associated macrophages within the TIME  
68 correlates with worse progression free survival (PFS) (10). Recently, spatial transcriptomics have  
69 proven to be a powerful tool to characterize the architecture of HGSC tumors, but these studies  
70 are currently performed with a limited spatial resolution (i.e., not single cell). These studies are  
71 also limited by their dependence on RNA expression (11–13). On the other hand, single cell

72 sequencing of HGSC tumors provides significantly improved resolution of the TIME but is  
73 limited by the lack of associated spatial context (14). Recent studies have demonstrated that,  
74 beyond TIME composition, the spatial organization of the TIME, including the proximity of  
75 macrophages, B cells, and CD4+ T-cells to tumor cells significantly correlates with survival  
76 outcomes (15). However, these studies relied on a limited number of proteins to characterize the  
77 TIME spatial organization and thus were lacking simultaneous cell type identification, and the  
78 associations were not validated with modern large predictive models. Research in other types of  
79 cancer, such as melanoma, has shown that spatial features derived from single-cell image data  
80 are associated with treatment response (16).

81         In this study, we determined the prognostic power of the TIME's spatial organization in  
82 explaining and predicting patient outcomes. Towards this end, we examined formalin-fixed  
83 paraffin-embedded (FFPE) tissue samples from 83 HGSC tumors from patients diagnosed with  
84 high grade serous carcinoma of the ovary, fallopian tube, and peritoneum with known outcomes  
85 with a multiplexed ion beam imaging (MIBI) system (17) and identified over 160,000 cells  
86 across 23 cell types. The resulting data set is one of the largest protein-based spatially intact,  
87 single cell analysis of any tumor type. Using survival and recurrence outcomes as an endpoint for  
88 77 (69 primary and 8 recurrent) of the samples that met the inclusion criteria to produce spatial  
89 features, we performed modeling of 6 known clinical/immunohistochemical features (e.g.,  
90 BRCA-status), 24 TIME composition features, 69 TIME spatial features, and 117 TIME (spatial)  
91 network features to assess their correlation with and relative importance for predicting patient  
92 outcomes. We found significant univariate correlations and high relative importance in high-  
93 dimensional predictive models for several features encoding TIME spatial organization. While  
94 we were unable to reliably predict out-of-sample overall survival (OS) outcomes with these

95 features, we consistently predicted out-of-sample PFS, with the best model on average using a  
96 combination of features of the TIME composition and spatial organization. We demonstrate how  
97 moving beyond TIME composition to encode and assess features of TIME spatial organization,  
98 combined with a modern machine learning approach, can be used to improve hypothesis  
99 generation and testing to identify clinically relevant parameters for improving HGSC patient  
100 care.

101

## 102 **RESULTS**

### 103 **Multiplexed imaging, cell segmentation, and phenotyping**

104 We performed multiplexed imaging using a custom MIBI-TOF instrument (17) to  
105 produce a total of 83 images identifying 26 proteins (File D1), which were processed using  
106 Ionpath's MIBI/O software and corrected (Table S1) and denoised (File D2). Multiplexed  
107 imaging data were preprocessed to remove noise and artifacts as described previously (26) prior  
108 to single-cell segmentation. In this preprocessing step, we used supervised pixel classification to  
109 generate a feature representation map for each image (Fig. 1A). We then applied a widely used  
110 pre-trained model (27) to perform whole-cell segmentation. This process identified about  
111 160,000 cells with each FOV containing an average of ~1934 single cells (s.d=556). The  
112 unsupervised clustering algorithm FlowSOM (28) was then employed, identifying 23 unique cell  
113 clusters (Fig. 1B,C, Fig. 2A). The cell type identity of each cluster was determined by comparing  
114 relative phenotypic marker signal intensities across clusters.

### 115 **Generating TIME composition features**

116 We first examined the TIME composition of the samples in terms of the relative  
117 frequency of cell types. This composition spanned 24 features of the samples exclusive of spatial

118 organization, comprising 23 cell types and the population of unidentified cells. We observed  
119 substantial variation in cell type frequencies across samples (Fig.2B). Tumor cells were the most  
120 prevalent cell type, representing on average 47.8% of the cells in each sample (range 0% to  
121 91.6%). The next most common cell types on average were neuroepithelial cells (mean 6.4%,  
122 range 0% to 61.5%; vs. tumor cell percentage, Pearson correlation coefficient  $r=-0.328$ , false  
123 discovery rate adjusted two-sided  $p=0.012$ ). All other cell types varied from 0% to 3.3% of the  
124 cells on average, though these percentages could vary dramatically between samples, often in  
125 relation to tumor cell percentage. Other cell types with false discovery rate adjusted significant  
126 correlation coefficients with tumor cell percentages were CD8+ T cells ( $r=-0.311$ ,  $p=0.013$ ),  
127 CD4+ T cells ( $r=-0.379$ ,  $p<0.001$ ), NK/NKT cells ( $r=-0.303$ ,  $p=0.014$ ), CD56+CD45- cells ( $r=-$   
128  $0.401$ ,  $p<0.001$ ), vascular endothelial cells ( $r=-0.29$ ,  $p=0.018$ ), B cells ( $r=-0.339$ ,  $p=0.009$ ),  
129 monocytes ( $r=-0.288$ ,  $p=0.018$ ), CD11c<sup>low</sup> immune cells ( $r=-0.28$ ,  $p=0.021$ ), neutrophils  
130 ( $r=-0.257$ ,  $p=0.036$ ), and CD11c+ epithelial cells ( $r=0.328$ ,  $p=0.009$ ). All other cell types did  
131 not have significant correlations (File D3). Some cell types such as dendritic cells (DC) and  
132 CD11c<sup>low</sup> immune cells were always rare, if present in a sample.

133 We excluded some samples from further analysis based on cell type percentages and two  
134 exclusion criteria (Fig. S1). Unidentified cells represented on average 16.7% of the cells in each  
135 sample (range 0.5% to 92.6%;  $r=-0.498$ ,  $p<0.001$ ). Samples 26 and 45 were excluded because  
136 they were outliers with unidentified cell percentages over 65%. Samples 27 and 29 were  
137 excluded because they had no identified tumor cells (sample 45 also met this exclusion criteria).  
138 We determined that samples with a high percentage of unidentified cells or no identified tumor  
139 cells were unable to produce spatial features about the interactions between cells of different  
140 types, and in particular interactions with tumor cells. In the two cases in which there were two

141 samples from the same patient, we chose to keep the sample with a lower unidentified cell  
142 percentage in the final analysis, thus excluding samples 19 and 35. This choice ensured that our  
143 final dataset included at most one sample from each patient in the analysis linking generated  
144 features to patient outcomes. In total, we excluded 6 samples from the final analysis, leading to a  
145 final dataset of 77 samples.

146 Most cell types were not represented across all images in the final dataset (Fig. 2C).  
147 Tumor cells were identified in every sample, and vascular endothelial cells, M1 macrophages,  
148 CD163+ cells, and Fibroblast cells were identified in almost every sample. Some cell types were  
149 rarer, particularly M2 macrophages, non-leukocyte derived neural cells, lymphatic endothelial  
150 cells, and dendritic cells were identified in fewer than half of the samples.

### 151 **Generating spatial features of the TIME based on nearest neighbor distances**

152 For each sample in the final dataset, we generated a set of 69 features that characterize  
153 each sample's spatial structure, following the approach from Moldoveanu et al. (2022) (16).  
154 First, we generated the median Euclidean distance from three distinct cell types ("focal cell  
155 types") that have been reported to be important in the HGSC TIME (tumor cells, M1  
156 macrophages, and vascular endothelial cells) in each sample to their nearest neighbors of each  
157 other cell type. While there have been few studies interrogating the spatial features of the TIME,  
158 previous work indicates that the spatial proximity between cell types correlates with HGSC  
159 survival outcomes (15). Previous results on composition (10,38,39), led us to focus on M1  
160 macrophages and vascular endothelial cells as focal cell types for generating spatial and network  
161 features along with tumor cells in our study. Vascular endothelial cells and M1 macrophages  
162 were also both detected in nearly all (98%, only missing in one sample each respectively)  
163 samples.

164 Tumor cells, vascular endothelial cells, M1 macrophages, CD163+ cells, and fibroblasts,  
165 which were some of the most common cell types across samples, were closer (average median  
166 nearest neighbor distance under 90  $\mu\text{m}$ ) than other cell types to all three focal cell types (Fig.3A-  
167 C). In comparison, the cell types that were in fewer samples (e.g., M2 macrophages, non-  
168 leukocyte derived neural cells, lymphatic endothelial cells, dendritic cells) were found on  
169 average further away from the three focal cell types. B cells had the highest mean nearest  
170 neighbor distance across samples to all three focal cell types (197.2  $\mu\text{m}$  to Tumor cells, 190.4  $\mu\text{m}$   
171 to M1 macrophages, and 174.2  $\mu\text{m}$  to vascular endothelial cells, respectively).

### 172 **Generating features of the TIME based on spatial network representations**

173 We next created spatial network representations of the samples by connecting spatially  
174 proximate cells using Delaunay triangulation and then trimming edges that were above a  
175 threshold of 50 pixels ( $\sim 24.4 \mu\text{m}$ ) (Fig. S2A-C). Cells were thus found 15-50 pixels ( $\sim 7.3$ - $24.4$   
176  $\mu\text{m}$ ) away from their spatial neighbors in the networks, with some variation in the median  
177 distances between spatial network neighbors based on their cell type (Fig. S3). Using these  
178 spatial network representations, we generated 117 TIME network features for each sample. The  
179 first subset of these features represented the mean size of connected regions of each cell type in  
180 each sample (Fig. S2D). These spatially connected regions in the TIME may indicate the  
181 existence of spatially extended structures of a single cell type (which may indicate the level of  
182 tumor infiltration, per Keren et al. 2018 (30)). Tumor cells were most often found in large,  
183 connected regions with 50% located in regions of 1071 cells or greater. Neuroepithelial cells  
184 were also found in relatively large, connected regions, with 50% found in regions of 226 cells or  
185 greater. Cells of all other types were most often found in relatively small regions ranging from 1  
186 to 14 cells (Fig. S4A). Most regions of any cell type were only 1 or 2 cells large. The largest



187 maximum region sizes were for tumor cells (2190 cells), Neuroepithelial cells (1288 cells),  
188 CD11b+ epithelial cells (349 cells), and CD4+ T cells (202 cells), while all other cell types had  
189 maximum region sizes under 200 cells (Fig. S4B).

190 We used the spatial network representations to compute contact enrichment scores,  
191 following prior work (30) (16) (31) to quantify the extent to which network-neighbors of focal  
192 cell types might differ from what should be expected at random. These scores capture similar  
193 proximity information as the median nearest neighbor distance features, but control for the  
194 proportion of cells of each type by keeping these proportions fixed during computation.  
195 Moreover, these scores quantify direct interactions between cell types.

196 Vascular endothelial cells, fibroblasts, and CD56+CD45- cells had fewer contacts with  
197 tumor cells than expected based on random sampling (null expectations), whereas CD11c+  
198 epithelial cells, CD11b+ epithelial cells, and neuroepithelial cells often had more contacts than  
199 expected. Most other cell types varied across samples with many contact enrichment scores close  
200 to 0, and thus matching null expectations (Fig. 3D). Most of the cell types showed slightly more  
201 contacts with M1 macrophages than expected at random (contact enrichment scores  $> 0$ ), with  
202 the exception of tumor cells and neuroepithelial cells, which tended to have fewer (contact  
203 enrichment scores  $< 0$ ) and other immune cells, B cells, NK/NKT cells, CD56+CD45- cells, non-  
204 leukocyte derived neural cells, and dendritic cells which tended to have contact enrichment  
205 scores with M1 macrophages close to 0 (Fig. 3E). Contact enrichment scores with vascular  
206 endothelial cells were also slightly positive for most cell types and negative for tumor cells.  
207 Fibroblasts had more contacts with vascular endothelial cells than expected at random and cell  
208 types with slightly negative or varying vascular endothelial contact enrichment scores included

209 CD11c+ epithelial cells, neuroepithelial cells, CD56+CD45- cells, and lymphatic endothelial  
210 cells (Fig.3F).

211 Finally, we generated assortativity coefficients from the spatial networks, which measure  
212 the extent to which cells tend to be network neighbors with cells of the same type as opposed to  
213 neighbors of any other type. These features capture similar information about large-scale  
214 structure and tumor infiltration as the mean region size, but better account for random variation.  
215 Tumor cells had the highest mean assortativity coefficient (0.37). We did not observe any cells  
216 exhibiting a negative assortativity coefficient (disassortative mixing), in which cells of a given  
217 cell type would be less likely to be network neighbors with same-type cells and more likely to be  
218 neighbors of different-type cells. We did, however, see large variation across samples in the  
219 magnitude of the assortativity coefficient for many cell types. For instance, the tumor cells  
220 displayed a large range of assortativity coefficients, which may indicate that the tumors in some  
221 samples were more infiltrated by other cells (Fig. 4).

## 222 **Linking in-sample patient outcomes to TIME features in univariate and multivariate Cox** 223 **regressions**

224 We next explored the relationship between generated features of the samples and two  
225 time-to-event outcomes: overall survival (OS) and progression-free survival (PFS) (Fig. S5, Fig.  
226 S6). We define OS as the time from initial diagnosis based on tissue biopsy and imaging or a  
227 serum biomarker (CA125) to death. Patient data without observation of death are censored at the  
228 last known patient visit. PFS is defined as the time from initial diagnosis to first known disease  
229 recurrence. Patient data without observation of disease recurrence are censored at death or the  
230 last known patient visit, whichever occurs first.

231 We performed Univariate Cox regressions for all the generated TIME composition,  
232 spatial, and network features as well as 6 additional clinical/immunohistochemical features: age,  
233 BRCA mutational status, H3K14Ace status, ATF6 status, DUSP1 status, and CBX2 status (see  
234 Fig. S7 for clinical/immunohistochemical feature distributions). All covariates except BRCA  
235 mutational status and age were first normalized (z-score scaled) so that they had a mean of 0 and  
236 a standard deviation of 1. Results limiting the dataset to only primary tumor samples can be  
237 found in Figure S8 and File D4.

238 For OS, we found significant univariate results ( $p < 0.05$ ) for 25 features associated with  
239 worse prognosis and 3 features associated with better prognosis (Fig. 5A, see File D5 for full  
240 results). For PFS, we found significant results ( $p < 0.05$ ) for eight features associated with worse  
241 prognosis and three features associated with better prognosis (Fig. 5B, see File D5 for full  
242 results). None of the clinical/immunohistochemical attributes were significant for either outcome  
243 variable.

244 Of the significant features, a majority were related to proximity between cells of  
245 particular types – median nearest neighbor distance features accounted for 18 of the 28  
246 significant features for OS and two of the 11 significant features for PFS. Contact enrichment  
247 features accounted for five of the 28 significant features for OS and seven of the 11 significant  
248 features for PFS. Relatively fewer of the significant features related to composition or the  
249 tendency for cells of the same type to cluster together – three composition features were  
250 significant for OS and one composition feature was significant for PFS, one mean region size  
251 feature was significant for OS, and none were significant for PFS, and one assortativity  
252 coefficient feature was significant for each of OS and PFS.

253 As a robustness check, we trained a set of reduced models, in the form of multivariate  
254 Cox regressions on only the top five features for each outcome variable ranked by  $p$ -value, with  
255 and without adjusting for the 6 clinical/immunohistochemical features (Table S2, S3). In the  
256 adjusted multivariate model for OS, none of the five top features remained significant, while in  
257 the reduced model the only feature that remained significant was the median NK/NKT cell  
258 nearest neighbor distance to vascular endothelial cells (Hazard Ratio [HR] =1.66,  $p=0.009$ ). For  
259 PFS, the only feature that remained significant in the adjusted model was the contact enrichment  
260 score between unidentified cells and M1 macrophages (HR=1.63,  $p=0.010$ ), while in the reduced  
261 model four of the top five features remained significant while the contact enrichment score  
262 between unidentified cells and M1 macrophages was not significant (HR=1.32,  $p=0.059$ ).

### 263 **Predicting out-of-sample patient outcomes using TIME features in random forests**

264 We next evaluated how spatial and/or network features of the tumor microenvironment  
265 could be used together with clinical/immunohistochemical attributes and TIME composition  
266 features to predict patient outcomes out-of-sample. We split both OS and PFS outcome variables  
267 at their respective medians to consider a simple binary classification task of low or high OS or  
268 PFS. We grouped features into 4 categories according to their respective processes of derivation:  
269 (i) clinical/immunohistochemical, (ii) composition, (iii) spatial, and (iv) network features. We  
270 considered all 15 possible combinations of the four feature categories to evaluate what  
271 combination of information produced the best out-of-sample predictive performance (Fig. 6A).

272 For each model, we repeatedly ( $N=500$ ) trained a random forest model on a training set  
273 of 70% of the samples, randomly sampled while balancing outcome labels, and evaluated each  
274 model's predictive accuracy by using the remaining 30% as a test set. We report average out-of-  
275 sample predictive performance results, based on the AUC (Area Under the Receiver Operating

276 Characteristics curve) statistic (36) across these 500 evaluations. A value of AUC=0.5 indicates a  
277 classification that performs no better or worse than a random guess, while an AUC=1 indicates  
278 perfect performance.

279         Across these predictive models, we found better-than-random performance on average,  
280 with AUC>0.5 for PFS but not for OS (Fig. 6B, C, Table S4). All models for PFS achieved mean  
281 AUC values over 0.6. The model that best predicted PFS was model eight, with AUC  $0.711 \pm$   
282  $0.10$  (mean  $\pm$  stddev) based on combining composition and spatial features. This performance  
283 was followed closely by model 11 ( $0.707 \pm 0.09$ ) and model 3 ( $0.703 \pm 0.08$ ), which used only  
284 spatial and a combination of clinical/immunohistochemical, composition, and spatial features,  
285 respectively. Models containing network features performed slightly worse (models 4, 7, 9, 10,  
286 12, 13, 14, 15; average AUC=  $0.668 \pm 0.03$ ) than models with clinical/immunohistochemical  
287 features (models 1, 5, 6, 7, 11, 12, 13, 15; average AUC= $0.678 \pm 0.03$ ), composition features  
288 (models 2, 5, 8, 9, 11, 12, 14, 15, average AUC= $0.690$ ), and spatial features (models 3, 6, 8, 10,  
289 11, 13, 14, 15; average AUC= $0.698 \pm 0.01$ ). The model containing all features (model 15)  
290 achieved an AUC of  $0.697 \pm 0.09$ . All the models predicting OS achieved mean AUC<0.5,  
291 indicating that on average the models did not outperform a random guess, i.e., they predicted in  
292 the incorrect direction (Fig. 5B). Similar performance results were found for models trained only  
293 on primary tumor samples (n=69), although composition features were relatively more helpful in  
294 predicting PFS, such that the top three models were model five ( $0.729 \pm 0.09$ ), model two ( $0.719$   
295  $\pm 0.09$ ), and model eight ( $0.714 \pm 0.09$ ) (Fig. S9, Table S5).

296         Using model 15, which was trained on all four feature categories, we generated  
297 hypotheses of which particular TIME composition, spatial, and network features were relatively  
298 more useful for predicting OS and PFS patient outcomes. We accomplished this goal by

299 calculating and comparing the Gini importance scores (37) for each feature in model 15. We note  
300 that importance scores do not indicate the direction of a feature's relationship with a patient's  
301 outcome, and instead only indicate its relative utility in predicting the outcome value. We found  
302 evidence for a subset of features, spanning all four categories, that were relatively more  
303 important for predicting patient outcomes (Fig. 7A,B). Feature importance results limiting the  
304 dataset to only primary tumor samples can be found in Figure S10 and File D6.

305         Ranking features by their median Gini importance score across the 500 evaluations, we  
306 found that the top ten features for predicting OS included seven contact enrichment network  
307 features, two spatial features, and one clinical/immunohistochemical feature: (i) the contact  
308 enrichment score between CD8<sup>+</sup> T cells and tumor cells, (ii) the contact enrichment score  
309 between CD163<sup>+</sup> cells and tumor cells, (iii) median monocyte cell nearest neighbor distance to  
310 tumor cells, (iv) median CD11c<sup>+</sup> epithelial cell nearest neighbor distance to tumor cells, (v) the  
311 contact enrichment score between NK/NKT cells and vascular endothelial cells, (vi) the contact  
312 enrichment score between CD11b<sup>+</sup> epithelial cells and M1 macrophages, (vii) the contact  
313 enrichment score between other immune cells and tumor cells, (viii) the contact enrichment score  
314 between CD11c<sup>+</sup> epithelial cells and vascular endothelial cells, (ix) CBX2 status, and (x) the  
315 contact enrichment score between unidentified cells and M1 macrophages (Fig. 7C, File D7).  
316 The contact enrichment score between CD8<sup>+</sup> T cells and tumor cells were distinguished by a  
317 higher median feature importance score.

318         We found that the top ten features for predicting PFS included one contact enrichment  
319 network feature, one mean region size network feature, five spatial features, and three  
320 composition features: (i) median vascular endothelial cell nearest neighbor distance to tumor  
321 cells, (ii) the contact enrichment score between unidentified cells and M1 macrophages, (iii)

322 median vascular endothelial cell nearest neighbor distance to M1 macrophages, (iv) vascular  
323 endothelial cell proportion, (v) median B cell nearest neighbor distance to vascular endothelial  
324 cells, (vi) CD4<sup>+</sup> T cell proportion, (vii) median CD163<sup>+</sup> cell nearest neighbor distance to tumor  
325 cells, (viii) M1 macrophage proportion, (ix) median CD11c<sup>+</sup> epithelial cell nearest neighbor  
326 distance to tumor cells, and (x) the CD4<sup>+</sup> T cell mean region size (Fig. 7D, File D7). In  
327 particular, for PFS the median vascular endothelial cell nearest neighbor distance to tumor cells  
328 was consistently ranked as more important across the iterations.

329 In alignment with the in-sample Cox regression results, we found that most of the top ten  
330 most important features for predicting out-of-sample patient outcomes (nine for OS and six for  
331 PFS) were either median nearest neighbor distances or spatial network contact enrichment  
332 scores, and thus related to the spatial proximity between cell types, and in general, features  
333 related to spatial proximity were more important (Fig. S11, Fig. S12).

### 334 **Results related to T cell, macrophage, B cell, and vascular endothelial cell spatial** 335 **organization**

336 Previous work has indicated that the presence of intratumoral T cells and the presence of  
337 T cells in ascites have been shown to correlate with better patient prognosis (8,15,40–42). High  
338 CD4<sup>+</sup> T cell macrophage interaction has also been shown to significantly correlate with better  
339 prognosis when adjusted for clinical/immunohistochemical covariates (15). In our results,  
340 patients with NK/NKT and CD4<sup>+</sup> T cells closer to M1 macrophages and tumor cells and  
341 NK/NKT cells closer to vascular endothelial cells had better OS, and the contact enrichment  
342 score between CD8<sup>+</sup> T cells and tumor cells was the most important feature for predicting OS.  
343 For PFS, the same features were not significantly correlated with prognosis, though NK/NKT  
344 cell M1 median nearest neighbor distance was significantly correlated with PFS for only primary

345 tumor samples (HR=1.43, p=0.038). We also saw a significant correlation for CD8+ T cell  
346 assortativity (HR 1.34, p=0.034, not significant for only primary tumor samples), and the CD4+  
347 T cell mean region size was chosen as an important feature for the random forest predicting PFS  
348 and was significantly correlated with PFS for only the primary tumor samples (HR 0.73,  
349 p=0.046), indicating that T cell clustering patterns might have been more important for  
350 predicting PFS than T cell spatial proximity features.

351 Macrophages compose up to 50% of all immune cells in the TIME and are a highly  
352 plastic cell type (6). As opposed to M2-like macrophages, M1-like macrophages are proposed to  
353 be anti-tumorigenic and aid the adaptive immune cells in mounting an immune response (43).  
354 The M1/M2 ratio of macrophages in the ovarian cancer TIME is prognostic for overall and  
355 progression-free survival (10,38,44). For macrophages, our significant results all were related to  
356 M1 macrophages rather than related to M2 macrophages. We found that higher median M1  
357 macrophage nearest neighbor distance to tumor cells (HR 1.25, p=0.039) or vascular endothelial  
358 cells (HR=1.34, p=0.021, not significant for only primary tumor samples) were significantly  
359 correlated with worse OS. Median vascular endothelial cell nearest neighbor distance to M1  
360 macrophages was also chosen as an important feature by the random forest for predicting PFS.

361 We found, in alignment with previous results (15) that a higher contact enrichment score  
362 between B cell and M1 macrophages was significantly correlated with both better OS  
363 (HR=0.696, p=0.011) and PFS (HR=0.73, p=0.039), and that a larger median B cell nearest  
364 neighbor distance to M1 macrophages was significantly correlated with worse OS (HR=1.40,  
365 p=0.016, not significant for only primary tumor samples). Unlike in Steinhart et al. 2021 (15) we  
366 differentiated between M1 and M2 macrophages, replicating this result for the former and thus  
367 adding further cell type specificity to these findings. These findings highlight that interaction



368 between B cells and M1 macrophages may lead to a better antitumor immune response after  
369 chemotherapy treatment potentially through increased macrophage-mediated antigen  
370 presentation to the B cells. We generally observed that B cells being further from M1  
371 macrophages, vascular endothelial cells, and tumor cells corresponded to worse outcomes -  
372 higher median B cell nearest neighbor distance to tumor cells (HR=1.42, p=0.008) or vascular  
373 endothelial cells (HR=1.33, p=0.042, not significant for only primary tumor samples) also  
374 significantly correlated with worse OS, and median B cell nearest neighbor distance to vascular  
375 endothelial cells was also significantly correlated with worse PFS (HR=1.35, p=0.030) and was  
376 chosen as an important feature for predicting PFS.

377 A higher density of microvessels in the TIME has also previously been correlated with  
378 worse progression-free survival (39), and anti-angiogenic therapies (e.g., anti-VEGF) are a  
379 standard of care for ovarian cancer. In our results, OS was significantly correlated (HR=1.23,  
380 p=0.073) with the median nearest neighbor distance between vascular endothelial cells and  
381 tumor cells, as in a higher median nearest neighbor distance between these cell types conveyed a  
382 worse OS. Median vascular endothelial cell nearest neighbor distance to tumor cells was also  
383 chosen as the most important feature for predicting PFS.

384

## 385 **DISCUSSION**

386 The current study provides a roadmap for further hypothesis generation and evaluation in  
387 ovarian cancer research, opening a range of possible directions for future work investigating the  
388 mechanisms by which TIME spatial organization drives clinical and biological differences.

389 Our results reinforce the importance of considering the spatial structure of the TIME to  
390 understand and predict HGSC disease progression and outcomes. We show that features

391 encoding the spatial and network organization of the TIME help predict patient outcomes, and  
392 we find that the best predictive model for PFS includes a combination of TIME composition and  
393 spatial features. For example, we found several results related to CD163+ cells, e.g., higher  
394 median CD163+ cell nearest neighbor distance to M1 macrophages correlated with worse OS  
395 (HR=1.31, p=0.022) and higher median CD163+ cell nearest neighbor distance to tumor cells  
396 correlated with worse PFS (HR=1.26, p=0.042) and was chosen as an important feature for  
397 predicting PFS. CD163 is a scavenger receptor, and its expression is largely restricted to  
398 myeloid-derived cells, specifically monocytes and macrophages – it is often upregulated in  
399 response to inflammation and is associated with tumor promoting macrophages (45). While  
400 CD163+ cells in the ovarian TIME are associated with worse prognosis (10,46,47), our findings  
401 show a spatial and context dependency on CD163-mediated activities. Therapeutically, CD163  
402 targeting strategies (e.g., OR2805) have shown to be effective in relieving immune suppression  
403 and are therefore clinically evaluated in a trial for solid tumors (48), thus representing an  
404 opportunity to target the robust HGSC TIME-associated immune suppressive macrophages to  
405 potentially improve anti-tumor immune surveillance (49,50).

406         While our results partially align with previous studies, for example in the finding for B  
407 cell-M1 macrophage interactions, we did not achieve significance in univariate correlations to  
408 patient outcomes for T cell and macrophage proportions as expected. While we did find Hazard  
409 Ratio estimates in the expected direction (Hazard Ratio estimates for infiltration by all T cell  
410 populations and M1 macrophages were <1), our results were not significant. Notably, increased  
411 CD8+ T cells conveyed a Hazard Ratio of 0.74 (p=0.059) and CD8+ T cell proportion (HR 0.68,  
412 p=0.035) and CD4+ T cell proportion (HR 0.58, p=0.02) were significantly correlated with  
413 improved OS for only the primary tumor samples. The vascular endothelial cell proportion, M1

414 macrophage proportion, and CD4+ T cell proportion were also chosen by the random forest as  
415 important features for predicting PFS. We emphasize the importance of differences in the  
416 definitions of cell types when comparing our results with previous works. For example, prior  
417 literature has suggested that M2 macrophages are typically more prevalent than M1 macrophages  
418 in HGSC (51), which contrasts with our results (Fig. 2A). However, if we had included CD163+  
419 cells in the M2 macrophage cluster (52,53), then the M2 macrophage count would indeed be  
420 higher than the M1 macrophage count alone and present findings in line with the aforementioned  
421 study. An explanation for differences with previous studies might be due to differences in cell  
422 clustering and phenotyping, pointing to the need for further refinement of consistent markers,  
423 particularly so that such results can become relevant in clinical application.

424         Limitations of the imaging technology used in this study affect the significance of our  
425 findings. In particular, the FOV size of 500  $\mu\text{m}$  at single-cell resolution might still be a limiting  
426 factor for the comprehensive documentation of the clinically relevant spatial organization in the  
427 TIME. Despite staining with antibodies to 26 proteins, an average of 14% of cells remained  
428 unidentified in the 77 samples included in our final analysis, due to them not expressing any of  
429 the phenotypic markers. The spatial organization of the TIME may be better delineated in a more  
430 comprehensive higher parameter analysis tailored to identification of cells in HGSC. For  
431 example, future work might additionally use functional markers to further characterize CD163+  
432 cells. In our analyses we treated the set of unidentified cells as a population and found that they  
433 contributed to significant interactions, highlighting an opportunity for future research. For  
434 example, the contact enrichment score between unidentified cells and M1 macrophages was  
435 significantly associated with worse PFS (HR=1.41, p=0.01) and chosen as one of the most  
436 important features for predicting both OS and PFS.

437 Our study investigated the relative importance of different types and combinations of  
438 clinical/immunohistochemical and TIME features in modeling patient outcomes before treatment  
439 via both feature importance values within a random forest model for out-of-sample prediction  
440 and coefficient values within Cox regressions on in-sample data. While one tumor sample was  
441 from 1996, and aspects of clinical management have improved over the time period during  
442 which the samples were generated (e.g., increased testing for BRCA mutation), we assume that  
443 better prognosis in this dataset largely is due to differential response to a standard of care  
444 treatment, which has not changed substantially since 1996. Cox regressions evaluated on in-  
445 sample data can be used to describe observed patterns, but do not provide results about out-of-  
446 sample predictive performance relevant for generalizing our results to new patients in clinical  
447 contexts. We also primarily report results from univariate analyses which only consider features  
448 in isolation and multivariate Cox regressions with all significant features did not converge. Due  
449 to the exploratory nature of the study, we report non-adjusted p-values, and we found no  
450 significant univariate correlations with false discovery rate adjusted p-values (33).

451 Although random forests are a popular choice in predictive modeling, in part because of  
452 their built-in regularization controls for overfitting and their strong interpretability (34), all  
453 machine learning models are potentially vulnerable to overfitting. In our analysis, we did not  
454 observe substantially better-than-random out of sample predictive performance on patient OS on  
455 average, indicating that the features chosen as relatively important for predicting OS might have  
456 been used by the model to overfit (i.e., learn complex rules to fit to the training dataset that do  
457 not generalize to predictive performance on unseen data), and thus might be considered with  
458 more skepticism than those chosen as relatively important for predicting PFS. We took care to  
459 avoid cases in which the data used to evaluate or test the model's accuracy was not fully

460 independent of the data used to train the model, for example by imputing NA values separately  
461 in the train and test sets, which is one cause of overfitting. At the same time, our training data  
462 were derived from 77 of patients whose corresponding feature sets may not be fully  
463 representative of the underlying biology, implying that the reported predictive accuracies should  
464 be interpreted cautiously, and more weight should be placed on the inference that some features  
465 are relatively more important than others in the prediction of patient outcomes.

466 In comparing categories of features based on their respective processes of derivation, we  
467 found that models including features derived from spatial network representations of the TIME  
468 performed slightly worse. However, our results do support the continued use of spatial networks  
469 in quantifying and evaluating the TIME. Network features were the largest and most diverse  
470 category of features we evaluated (N=117), and many of them were irrelevant for predicting  
471 patient outcomes, as indicated by low Gini importance scores, thus likely reducing predictive  
472 performance for the network feature category as a whole by introducing noise. However, feature  
473 importance evaluations indicate that a subset of these network features were among some of the  
474 most important features overall for prediction: in particular, the contact enrichment features  
475 encoding information about the proximity between cell types were generally ranked as more  
476 important than mean region size or assortativity features, which encode cell clustering patterns  
477 (Fig. S11, Fig. S12), mirroring a similar finding in the in-sample Cox regression results. Further  
478 development and refinement of features derived from spatial network representations of the  
479 TIME could potentially improve the development of useful markers.

480 Many of the features identified as important for patient outcome prediction involved the  
481 spatial relationship between cells other than tumor cells. While not surprising, this finding  
482 strongly emphasizes the importance of investigating cell-cell interactions throughout the TIME.

483 Two overarching goals of such studies would be to (i) identify key cell types that can be directly  
484 addressed with targeted therapies, and (ii) to develop methods that more generally help to  
485 characterize the TIME prior to patient treatment. For instance, further studies might investigate  
486 how the spatial organization of the TIME differs between tumor sites within the same patient,  
487 and whether this can drive differential response to treatment between tumor sites (54).  
488 Additionally, future work could build on previous studies investigating TIME changes with  
489 chemotherapy treatment (55,56) to investigate how the spatial organization of the TIME changes  
490 with chemotherapy. Those goals aim to improve individualized patient diagnosis and care while  
491 at the same time enhancing our understanding of more general pathways of cancer development  
492 and progression.

493

## 494 **MATERIALS AND METHODS**

### 495 **Study design**

496 We procured formalin-fixed paraffin-embedded tumor samples from patients diagnosed  
497 with HGSC of the ovary, fallopian tube, and peritoneum under the University of Colorado's IRB  
498 Protocol, COMIRB #17-7788. The tumor samples were examined by a Gynecologic Pathologist  
499 (Dr. Miriam Post) and viable tumor areas were selected for generation of the tissue microarray.  
500 The total number of tumors on the tissue microarray was 133, which include primary and  
501 recurrent HGSC tumors. Further details of the tissue microarray can be found in Watson et al.  
502 2019 (18), Jordan et al. 2020 (19), and McMellen et al. 2023 (20). Multiplexed ion beam  
503 imaging was performed on 83 tumor specimens. All samples were from patients with cancer of  
504 ovary, fallopian tube, and peritoneum diagnosed at a similar stage (IIIC). For 77 (69 primary and  
505 8 recurrent) of these samples with sufficient cell type identification to produce spatial features

506 (see Fig. S1), we studied clinical/immunohistochemical features in combination with descriptive  
507 (composition, spatial, and network features) features derived from these samples. The study  
508 design aims to integrate features that could hypothetically be generated from a patient's biopsy  
509 samples before treatment in an exploratory analysis to investigate what features or combination  
510 of features could be used to predict patient outcomes and motivate adjustments in treatment.

### 511 **Clinical/immunohistochemical features**

512 For each sample, we investigated six clinical/immunohistochemical features alone and in  
513 combination with features derived from the samples: BRCA mutational status, age, and histology  
514 scores for H3K14Ace status, ATF6 status, DUSP1 status, and CBX2 status, calculated by  
515 multiplying the intensity of the stain [0-3] by the percentage of that intensity [0-100].

516 BRCA mutational status was included because of its well-established risk and therapeutic  
517 implication (21,22). The remaining features were selected and included based on prior work  
518 (20,23,24) that demonstrated prognostic value. Age was included because it is a prognostication  
519 indicator in terms of OS (25). Figure S7 shows distributions of all the  
520 clinical/immunohistochemical features across the final 77 samples analyzed.

### 521 **MIBI-TOF imaging**

522 Imaging was performed using a custom MIBI-TOF instrument with a Xe<sup>+</sup> primary ion  
523 source upgrade (17). A total of 83 images with a field of view size of 500×500 μm and a frame  
524 size of 1024×1024 pixels were acquired. The beam current was set to 5 nA with a dwell time of 2  
525 ms, yielding a resolution of approximately 0.5 μm per pixel. Secondary ions were accelerated  
526 into the time-of-flight mass spectrometer with a sample bias of 50 V and detected with a  
527 temporal resolution of 0.6 ns across a mass range of 1-200 m/z<sup>+</sup>.

### 528 **Low-level image processing**

529            Multiplexed images were extracted and processed using Ionpath's MIBI/O software: The  
530 image data was background- and mass-corrected with vendor-provided configuration files, see  
531 Table S1. In the next step, the image data was denoised with the filtering parameters provided in  
532 File D2.

### 533 **Low-level image pre-processing**

534            We adopted a custom computational pipeline developed to analyze MIBI data (26). In  
535 this framework multi-step low-level image processing is replaced with a single-step pixel  
536 classification where each pixel in an image is classified such that all categories of undesired  
537 signal are placed in a different class from the desired marker signal and continue the downstream  
538 analysis using the generated feature representation map of the marker signal.

### 539 **Single-cell segmentation**

540            Whole-cell segmentation was done using the pre-trained single-cell segmentation model  
541 Mesmer (27). We used the dsDNA channel for nuclear segmentation and the  $\beta$ -tubulin channel to  
542 guide identification of cell boundaries.

### 543 **Cell-type identification**

544            Single-cell data were extracted for all the cells and normalized by the cell size. To assign  
545 each cell to a lineage, we used the unsupervised clustering algorithm as implemented in  
546 FlowSOM (28) with multiple steps: first we identified the immune cells and non-immune cells  
547 using the following markers: CD45, HLA-DR, CD31, Podoplanin, Vimentin, and Keratin. Then,  
548 we used the immune markers CD3, CD4, CD8, CD20, CD68, CD56, CD11b, CD11c, CD163,  
549 DC-SIGN to identify the immune subsets (See Table S6).

### 550 **Spatial and network features**



551 We calculated spatial and network features from the sample images following  
552 Moldoveanu et al. 2022 (16) using Python version 3.9.12, *SciPy* version 1.7.3 and *NetworkX*  
553 version 2.7.1. We calculated the median Euclidean distance in pixels in each sample between  
554 cells of three focal cell types: tumor cells, M1 macrophages, and vascular endothelial cells and  
555 their nearest neighbor of all other non-focal cell types. In each sample, we examined each of the  
556 focal cells of interest and then identified the nearest neighbor of each non-focal cell type using  
557 KD Trees (implemented in *SciPy*) and recorded the Euclidean distances. For each sample, we  
558 report the median nearest neighbor distance for each combination of non-focal cell type (listed  
559 first) and focal cell type.

560 Spatial network representations of the samples were created by connecting spatial  
561 neighbors identified using Delaunay triangulation (implemented in *SciPy*) and then trimming  
562 edges that were above a threshold of 50 pixels (~24.4  $\mu\text{m}$ ). Results were not sensitive to using a  
563 higher threshold for trimming edges (100 pixels, ~48.8  $\mu\text{m}$ , Fig. S13-15). Versions of the spatial  
564 networks were created in which neighboring cells were only connected if they were of the same  
565 cell type and connected regions of the same cell type were identified from these modified  
566 networks using the `connected_components` function implemented in *NetworkX*. The mean of  
567 the region sizes in each sample were reported for each cell type.

568 Binary attributes were added to each cell in the spatial networks for each cell type, set to  
569 1 if the cell was of that type and 0 otherwise. Assortativity coefficients (29) were then calculated  
570 using the *NetworkX* function `attribute_assortativity_coefficient` for each of these  
571 binary cell type attributes, thus measuring to what extent cells tended to be neighbors with cells  
572 of the same type versus any other type. This value is 1 for perfect assortative mixing, in which  
573 cells are only neighbors with cells of the same type, 0 when there is no assortative mixing, and

574 negative when there is disassortative mixing, in which cells are typically neighbors with cells of  
575 different types.

576 We calculated contact enrichment scores for the three focal cell types of tumor cells, M1  
577 macrophages, and vascular endothelial cells and each non-focal cell type. Following a procedure  
578 used in prior work (16,30,31), the cell type labels of all cells other than those of the focal cell  
579 types were randomized 1000 times. After each shuffle, the number of times that the focal cell  
580 type was a neighbor of each non-focal cell type in the spatial network is recorded. These counts  
581 represent a null distribution for each non-focal cell type which is then compared to the observed  
582 number of contacts, and the z-score is recorded as the contact enrichment score. A negative  
583 contact enrichment score thus indicates fewer contacts than expected at random, a contact  
584 enrichment score of 0 indicates as many, and a positive contact enrichment score indicates more  
585 contacts than expected at random. When a cell type was missing from a sample, we recorded the  
586 mean region, contact enrichment and assortativity values as 0 and the median nearest neighbor  
587 distances as “NA” for features related to that cell type for the sample. We also report results for  
588 both the Cox regression and random forest analyses in the supplementary material when  
589 recording these values all as “NA” (See Note S1, File D8, Fig. S16-18).

## 590 **Statistical analysis**

591 We fit Cox proportional hazards regression models (32) to OS and PFS outcomes using  
592 the `coxph` function from the *survival* package (version 3.5-5) in R (version 4.3.1). Univariate  
593 regressions were performed with each of the 216 clinical/immunohistochemical, composition,  
594 spatial, and network features treated as individual covariates. All covariates except BRCA  
595 Mutation and age were z-score normalized before analysis so that coefficients were comparable  
596 across different feature scales and any rows with NA values were excluded. A covariate was

597 considered significant if it had a p-value of under 0.05. In the Supplementary Materials (File D5)  
598 we report the number of samples considered for each regression, the number of relevant events  
599 considered in the time to event analysis (death or recurrence, respectively), the covariate's  
600 coefficient in the Cox proportional hazard regression, the corresponding hazard ratio, and the p-  
601 value and false discovery rate adjusted p-value (33). Given the exploratory nature of this study,  
602 we focused on results that were significant with non-adjusted p-values. Multivariate Cox  
603 proportional hazards models were fitted using the `coxphmulti` function. Models with all  
604 covariates found to be significant in univariate regressions for both outcome variables did not  
605 converge, so we ran multivariate models with the top five features for each outcome variable,  
606 ranked by p-value, both adjusted for clinical/immunohistochemical attributes and as a reduced  
607 model without an adjustment for clinical/immunohistochemical attributes (Table S2, S3).

#### 608 **Predictive analysis**

609 We used a random forest classification model (34) implemented in the R package  
610 *randomForest* (version 4.7-1.1), R version 4.3.1 with default hyperparameters (see Note S2).  
611 Random forests were chosen as our predictive method because they have been shown to work  
612 well on high-dimensional data with a low sample size and can be used to rank features based on  
613 importance scores (35).

614 We first investigated what subsets of features, based on all possible combinations of the  
615 four feature categories (clinical/immunohistochemical, composition, spatial, and network  
616 features), produced the highest expected out-of-sample predictive performance: We repeated 500  
617 classification tasks for each of the two outcome variables and 15 models. For each of these  
618 classification tasks, 70% of the samples were treated as a training set and 30% were treated as a  
619 test set. Data was split randomly for each classification task using the `sample.split` function

620 in the package *caTools* (version 1.18.2) in order to preserve the ratio between outcome labels in  
621 the two sets. NA values were imputed separately in the training and test set using the  
622 `na.roughfix` function from the *randomForest* package which performs median substitution  
623 for numeric variables and mode substitution for factor variables. In the rare cases when a train  
624 and test split were selected such that a feature was entirely NA in the test set, we did not use that  
625 train-test split and instead re-drew. Predictive performance was calculated for each classification  
626 task using the AUC (Area under the receiver operating characteristics curve) statistic, calculated  
627 using the `roc` and `auc` functions in the *pROC* package, with the direction parameter set such that  
628 positive samples should receive a higher predicted value (version 1.18.2). The AUC statistic was  
629 chosen because of its properties of being threshold invariant, scale invariant, and use-case  
630 agnostic, hence providing a useful measure by which to compare the general performance of  
631 different models (36).

632         Second, we investigated an overall ranking of feature importance from the models  
633 including all features. Features were ranked based on their median Gini importance across the  
634 500 classification tasks. The Gini importance for a feature indicates the mean decrease in node  
635 impurity caused by splitting on that feature during model training, in which higher values  
636 indicate that the feature was more useful during the generation of the random forest model. The  
637 Gini importance can be biased to provide higher importance values for numeric features as they  
638 exhibit more potential split points (37). However, this bias would not have a strong influence on  
639 our results because the BRCA mutation status is the only categorical variable in our dataset.  
640 Repeating the evaluation 500 times allowed us to explore consistency and variation in the  
641 ranking of the features across different train and test splits of the data, which we chose to do

642 based on the small sample size and the expectation that many of the generated features would be  
643 highly correlated.

644

645 **Acknowledgements:** We acknowledge philanthropic contributions from Kay L. Dunton  
646 Endowed Memorial Professorship In Ovarian Cancer Research, the McClintock-Addlesperger  
647 Family, Karen M. Jennison, Don and Arlene Mohler Johnson Family, Michael Intagliata, Duane  
648 and Denise Suess, Mary Normandin, and Donald Engelstad. We thank Samreen Anjum for  
649 conversations about the predictive modeling. We thank Dr. Angelo's laboratory at Stanford for  
650 assistance with MIBI instrument setup and recording time. This work was supported by The  
651 American Cancer Society (B Bitler, RSG-19-129-01-DDC), NIH/NCI (B Bitler, R37CA261987  
652 and R01CA285446), and Ovarian Cancer Research Alliance (A Clauset and B Bitler), and the  
653 University of Colorado Cancer Center Support Grant (P30CA046934). We also thank the Human  
654 Immune Monitoring Shared Resource (RRID:SCR\_021985) for their expert assistance with  
655 sample preparation and data acquisition.

656

657 **Informed consent statement:** A TMA comprised of serous tumors (COMIRB #17-7788) was  
658 used. This protocol is deemed exempt, as it is using previously collected data, and the  
659 information is not recorded in a manner that is identifiable. Further, the findings of the study did  
660 not alter treatment choices or patient outcomes.

661

662 **Data availability statement:** Data and code used to perform analyses and supplemental data  
663 files are available upon request.

664

665 **References**

- 666 1. Lisio M-A, Fu L, Goyeneche A, Gao Z, Telleria C. High-Grade Serous Ovarian Cancer:  
667 Basic Sciences, Clinical and Therapeutic Standpoints. *IJMS*. 2019;20:952.
- 668 2. Siegel RL, Miller KD, Wagle NS, Jemal A. Cancer statistics, 2023. *CA A Cancer J*  
669 *Clinicians*. 2023;73:17–48.
- 670 3. Hoppenot C, Eckert MA, Tienda SM, Lengyel E. Who are the long-term survivors of high  
671 grade serous ovarian cancer? *Gynecologic Oncology*. 2018;148:204–12.
- 672 4. Garsed DW, Pandey A, Fereday S, Kennedy CJ, Takahashi K, Alsop K, et al. The genomic  
673 and immune landscape of long-term survivors of high-grade serous ovarian cancer. *Nat*  
674 *Genet*. 2022;54:1853–64.
- 675 5. Coscia F, Lengyel E, Duraiswamy J, Ashcroft B, Bassani-Sternberg M, Wierer M, et al.  
676 Multi-level Proteomics Identifies CT45 as a Chemosensitivity Mediator and  
677 Immunotherapy Target in Ovarian Cancer. *Cell*. 2018;175:159-170.e16.
- 678 6. Launonen I-M, Lyytikäinen N, Casado J, Anttila EA, Szabó A, Haltia U-M, et al. Single-  
679 cell tumor-immune microenvironment of BRCA1/2 mutated high-grade serous ovarian  
680 cancer. *Nat Commun*. 2022;13:835.
- 681 7. Kandalaft LE, Odunsi K, Coukos G. Immune Therapy Opportunities in Ovarian Cancer.  
682 *American Society of Clinical Oncology Educational Book*. 2020;e228–40.
- 683 8. Zhang L, Conejo-Garcia JR, Katsaros D, Gimotty PA, Massobrio M, Regnani G, et al.  
684 Intratumoral T Cells, Recurrence, and Survival in Epithelial Ovarian Cancer. *N Engl J Med*.  
685 2003;348:203–13.
- 686 9. Nielsen JS, Sahota RA, Milne K, Kost SE, Nesslinger NJ, Watson PH, et al. CD20+  
687 Tumor-Infiltrating Lymphocytes Have an Atypical CD27– Memory Phenotype and

- 688 Together with CD8+ T Cells Promote Favorable Prognosis in Ovarian Cancer. *Clinical*  
689 *Cancer Research*. 2012;18:3281–92.
- 690 10. Yuan X, Zhang J, Li D, Mao Y, Mo F, Du W, et al. Prognostic significance of tumor-  
691 associated macrophages in ovarian cancer: A meta-analysis. *Gynecologic Oncology*.  
692 2017;147:181–7.
- 693 11. Chen J, Wang Y, Ko J. Single-cell and spatially resolved omics: Advances and limitations.  
694 *Journal of Pharmaceutical Analysis*. 2023;13:833–5.
- 695 12. Williams CG, Lee HJ, Asatsuma T, Vento-Tormo R, Haque A. An introduction to spatial  
696 transcriptomics for biomedical research. *Genome Med*. 2022;14:68.
- 697 13. Fang S, Chen B, Zhang Y, Sun H, Liu L, Liu S, et al. Computational Approaches and  
698 Challenges in Spatial Transcriptomics. *Genomics, Proteomics & Bioinformatics*.  
699 2023;21:24–47.
- 700 14. Lee J, Yoo M, Choi J. Recent advances in spatially resolved transcriptomics: challenges  
701 and opportunities. *BMB Rep*. 2022;55:113–24.
- 702 15. Steinhart B, Jordan KR, Bapat J, Post MD, Brubaker LW, Bitler BG, et al. The Spatial  
703 Context of Tumor-Infiltrating Immune Cells Associates with Improved Ovarian Cancer  
704 Survival. *Molecular Cancer Research*. 2021;19:1973–9.
- 705 16. Moldoveanu D, Ramsay L, Lajoie M, Anderson-Trocme L, Lingrand M, Berry D, et al.  
706 Spatially mapping the immune landscape of melanoma using imaging mass cytometry. *Sci*  
707 *Immunol*. 2022;7:eabi5072.
- 708 17. Greenbaum S, Averbukh I, Soon E, Rizzuto G, Baranski A, Greenwald NF, et al. A  
709 spatially resolved timeline of the human maternal–fetal interface. *Nature*. 2023;619:595–  
710 605.

- 711 18. Watson ZL, Yamamoto TM, McMellen A, Kim H, Hughes CJ, Wheeler LJ, et al. Histone  
712 methyltransferases EHMT1 and EHMT2 (GLP/G9A) maintain PARP inhibitor resistance in  
713 high-grade serous ovarian carcinoma. *Clin Epigenet.* 2019;11:165.
- 714 19. Jordan KR, Sikora MJ, Slansky JE, Minic A, Richer JK, Moroney MR, et al. The Capacity  
715 of the Ovarian Cancer Tumor Microenvironment to Integrate Inflammation Signaling  
716 Conveys a Shorter Disease-free Interval. *Clinical Cancer Research.* 2020;26:6362–73.
- 717 20. McMellen A, Yamamoto TM, Qamar L, Sanders BE, Nguyen LL, Ortiz Chavez D, et al.  
718 ATF6-Mediated Signaling Contributes to PARP Inhibitor Resistance in Ovarian Cancer.  
719 *Molecular Cancer Research.* 2023;21:3–13.
- 720 21. Gori S, Barberis M, Bella MA, Buttitta F, Capoluongo E, Carrera P, et al.  
721 Recommendations for the implementation of BRCA testing in ovarian cancer patients and  
722 their relatives. *Critical Reviews in Oncology/Hematology.* 2019;140:67–72.
- 723 22. Moschetta M, George A, Kaye SB, Banerjee S. BRCA somatic mutations and epigenetic  
724 BRCA modifications in serous ovarian cancer. *Annals of Oncology.* 2016;27:1449–55.
- 725 23. Sanders BE, Yamamoto TM, McMellen A, Woodruff ER, Berning A, Post MD, et al.  
726 Targeting DUSP Activity as a Treatment for High-Grade Serous Ovarian Carcinoma.  
727 *Molecular Cancer Therapeutics.* 2022;21:1285–95.
- 728 24. Wheeler LJ, Watson ZL, Qamar L, Yamamoto TM, Post MD, Berning AA, et al. CBX2  
729 identified as driver of anoikis escape and dissemination in high grade serous ovarian cancer.  
730 *Oncogenesis.* 2018;7:92.
- 731 25. Peres LC, Sinha S, Townsend MK, Fridley BL, Karlan BY, Lutgendorf SK, et al. Predictors  
732 of survival trajectories among women with epithelial ovarian cancer. *Gynecologic*  
733 *Oncology.* 2020;156:459–66.



- 734 26. Ahmadian M, Rickert C, Minic A, Wrobel J, Bitler BG, Xing F, et al. A platform-  
735 independent framework for phenotyping of multiplex tissue imaging data. Uhlmann V,  
736 editor. PLoS Comput Biol. 2023;19:e1011432.
- 737 27. Greenwald NF, Miller G, Moen E, Kong A, Kagel A, Dougherty T, et al. Whole-cell  
738 segmentation of tissue images with human-level performance using large-scale data  
739 annotation and deep learning. Nat Biotechnol. 2022;40:555–65.
- 740 28. Van Gassen S, Callebaut B, Van Helden MJ, Lambrecht BN, Demeester P, Dhaene T, et al.  
741 FlowSOM: Using self-organizing maps for visualization and interpretation of cytometry  
742 data. Cytometry Pt A. 2015;87:636–45.
- 743 29. Newman MEJ. Mixing patterns in networks. Phys Rev E. 2003;67:026126.
- 744 30. Keren L, Bosse M, Marquez D, Angoshtari R, Jain S, Varma S, et al. A Structured Tumor-  
745 Immune Microenvironment in Triple Negative Breast Cancer Revealed by Multiplexed Ion  
746 Beam Imaging. Cell. 2018;174:1373-1387.e19.
- 747 31. Schapiro D, Jackson HW, Raghuraman S, Fischer JR, Zanotelli VRT, Schulz D, et al.  
748 histoCAT: analysis of cell phenotypes and interactions in multiplex image cytometry data.  
749 Nat Methods. 2017;14:873–6.
- 750 32. Andersen PK, Gill RD. Cox’s Regression Model for Counting Processes: A Large Sample  
751 Study. Ann Statist [Internet]. 1982 [cited 2023 Jul 31];10. Available from:  
752 [https://projecteuclid.org/journals/annals-of-statistics/volume-10/issue-4/Coxs-Regression-](https://projecteuclid.org/journals/annals-of-statistics/volume-10/issue-4/Coxs-Regression-Model-for-Counting-Processes--A-Large-Sample/10.1214/aos/1176345976.full)  
753 [Model-for-Counting-Processes--A-Large-Sample/10.1214/aos/1176345976.full](https://projecteuclid.org/journals/annals-of-statistics/volume-10/issue-4/Coxs-Regression-Model-for-Counting-Processes--A-Large-Sample/10.1214/aos/1176345976.full)
- 754 33. Benjamini Y, Hochberg Y. Controlling the False Discovery Rate: A Practical and Powerful  
755 Approach to Multiple Testing. Journal of the Royal Statistical Society: Series B  
756 (Methodological). 1995;57:289–300.

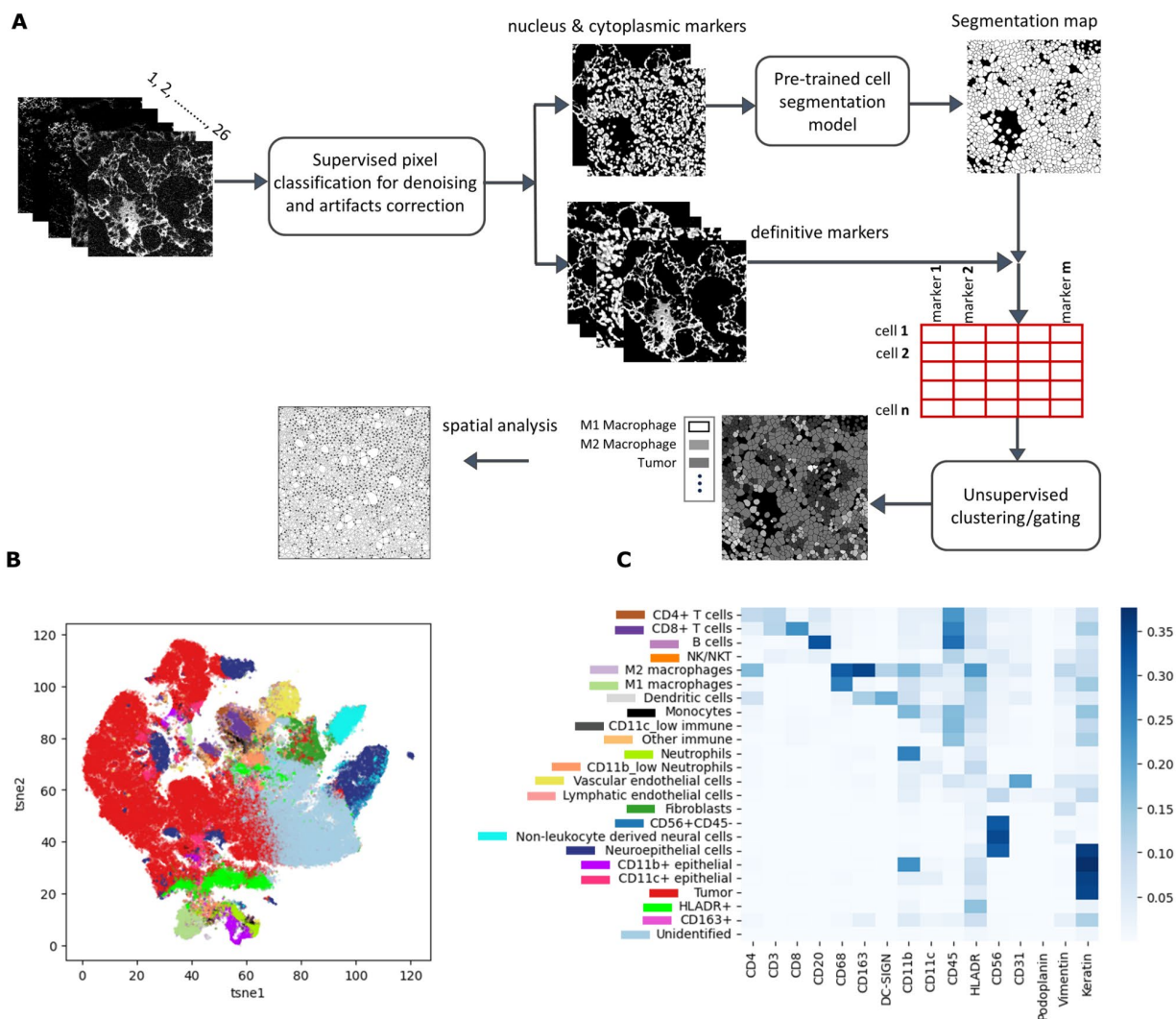
- 757 34. Breiman L. Random Forests. *Machine Learning*. 2001;45:5–32.
- 758 35. Chen X, Ishwaran H. Random forests for genomic data analysis. *Genomics*. 2012;99:323–9.
- 759 36. Fawcett T. An introduction to ROC analysis. *Pattern Recognition Letters*. 2006;27:861–74.
- 760 37. Nembrini S, König IR, Wright MN. The revival of the Gini importance? Valencia A, editor.  
761 *Bioinformatics*. 2018;34:3711–8.
- 762 38. Macciò A, Gramignano G, Cherchi MC, Tanca L, Melis L, Madeddu C. Role of M1-  
763 polarized tumor-associated macrophages in the prognosis of advanced ovarian cancer  
764 patients. *Sci Rep*. 2020;10:6096.
- 765 39. Rubatt JM, Darcy KM, Hutson A, Bean SM, Havrilesky LJ, Grace LA, et al. Independent  
766 prognostic relevance of microvessel density in advanced epithelial ovarian cancer and  
767 associations between CD31, CD105, p53 status, and angiogenic marker expression: A  
768 Gynecologic Oncology Group study. *Gynecologic Oncology*. 2009;112:469–74.
- 769 40. Pinto MP, Balmaceda C, Bravo ML, Kato S, Villarroel A, Owen GI, et al. Patient  
770 inflammatory status and CD4<sup>+</sup>/CD8<sup>+</sup> intraepithelial tumor lymphocyte infiltration are  
771 predictors of outcomes in high-grade serous ovarian cancer. *Gynecologic Oncology*.  
772 2018;151:10–7.
- 773 41. Mhaweche-Fauceglia P, Wang D, Ali L, Lele S, Huba MA, Liu S, et al. Intraepithelial T  
774 cells and tumor-associated macrophages in ovarian cancer patients. *Cancer Immunity*.  
775 2013;13.
- 776 42. Lieber S, Reinartz S, Raifer H, Finkernagel F, Dreyer T, Bronger H, et al. Prognosis of  
777 ovarian cancer is associated with effector memory CD8<sup>+</sup> T cell accumulation in ascites,  
778 CXCL9 levels and activation-triggered signal transduction in T cells. *OncoImmunology*.  
779 2018;7:e1424672.

- 780 43. Mantovani A, Marchesi F, Malesci A, Laghi L, Allavena P. Tumour-associated  
781 macrophages as treatment targets in oncology. *Nat Rev Clin Oncol*. 2017;14:399–416.
- 782 44. Zhang M, He Y, Sun X, Li Q, Wang W, Zhao A, et al. A high M1/M2 ratio of tumor-  
783 associated macrophages is associated with extended survival in ovarian cancer patients.  
784 2014;
- 785 45. Buechler C, Ritter M, Orsó E, Langmann T, Klucken J, Schmitz G. Regulation of scavenger  
786 receptor CD163 expression in human monocytes and macrophages by pro- and  
787 antiinflammatory stimuli. *Journal of Leukocyte Biology*. 2000;67:97–103.
- 788 46. No JH, Moon JM, Kim K, Kim Y-B. Prognostic Significance of Serum Soluble CD163  
789 Level in Patients with Epithelial Ovarian Cancer. *Gynecol Obstet Invest*. 2013;75:263–7.
- 790 47. Lan C, Huang X, Lin S, Huang H, Cai Q, Wan T, et al. Expression of M2-Polarized  
791 Macrophages is Associated with Poor Prognosis for Advanced Epithelial Ovarian Cancer.  
792 *Technol Cancer Res Treat*. 2013;12:259–67.
- 793 48. OncoResponse, Inc. A Phase 1-2 Study of OR2805, a Monoclonal Antibody Targeting  
794 CD163, Alone and in Combination With Anticancer Agents in Subjects With Advanced  
795 Malignancies [Internet]. *clinicaltrials.gov*; 2022 Sep. Report No.: NCT05094804. Available  
796 from: <https://clinicaltrials.gov/study/NCT05094804>
- 797 49. Chen T, Chen J, Zhu Y, Li Y, Wang Y, Chen H, et al. CD163, a novel therapeutic target,  
798 regulates the proliferation and stemness of glioma cells via casein kinase 2. *Oncogene*.  
799 2019;38:1183–99.
- 800 50. Probst P, Simmons R, Dinh H, Zuck M, Wall V, Bouchlaka M, et al. 271 Development of  
801 OR2805, an anti-CD163 antibody derived from an elite responder to checkpoint inhibitor

- 802 therapy that relieves immunosuppression caused by M2c macrophages. *J Immunother*  
803 *Cancer*. 2021;9:A294–A294.
- 804 51. Schweer D, McAtee A, Neupane K, Richards C, Ueland F, Kolesar J. Tumor-Associated  
805 Macrophages and Ovarian Cancer: Implications for Therapy. *Cancers*. 2022;14:2220.
- 806 52. Biswas SK, Mantovani A. Macrophage plasticity and interaction with lymphocyte subsets:  
807 cancer as a paradigm. *Nat Immunol*. 2010;11:889–96.
- 808 53. Sulahian TH, Högger P, Wahner AE, Wardwell K, Goulding NJ, Sorg C, et al. Human  
809 monocytes express CD163, which is upregulated by IL-10 and identical to p155. *Cytokine*.  
810 2000;12:1312–21.
- 811 54. Masoodi T, Siraj S, Siraj AK, Azam S, Qadri Z, Parvathareddy SK, et al. Genetic  
812 heterogeneity and evolutionary history of high-grade ovarian carcinoma and matched  
813 distant metastases. *Br J Cancer*. 2020;122:1219–30.
- 814 55. Mesnage SJL, Auguste A, Genestie C, Dunant A, Pain E, Drusch F, et al. Neoadjuvant  
815 chemotherapy (NACT) increases immune infiltration and programmed death-ligand 1 (PD-  
816 L1) expression in epithelial ovarian cancer (EOC). *Annals of Oncology*. 2017;28:651–7.
- 817 56. Cao G, Hua D, Li J, Zhang X, Zhang Z, Zhang B, et al. Tumor immune microenvironment  
818 changes are associated with response to neoadjuvant chemotherapy and long-term survival  
819 benefits in advanced epithelial ovarian cancer: A pilot study. *Front Immunol*.  
820 2023;14:1022942.
- 821

822 **Figures**

823



824

825 **Fig 1. Cell segmentation and phenotyping.** (A) Computational pipeline used for single-cell

826 segmentation and cellular phenotyping of the MIBI imaging data. The process starts with pixel

827 classification, where a pixel classifier distinguishes between two classes: Class I for desired

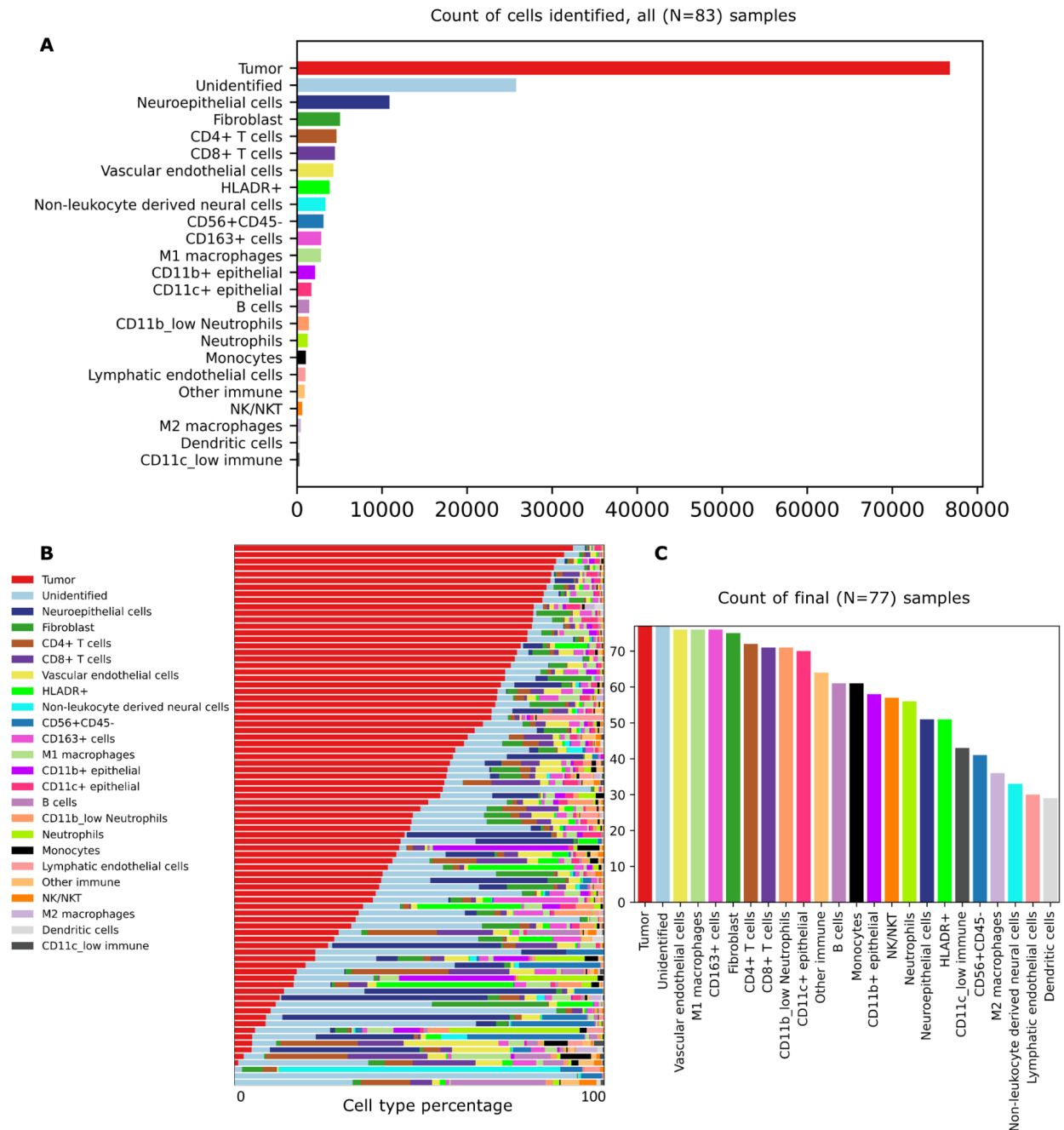
828 signals and Class II for noise and artifacts. The classifier's output produces feature representation

829 maps with pixel values scaled from 0 to 1. A pretrained single-cell segmentation model is used

830 for cell segmentation. Subsequently, marker expression within cell boundaries is quantified using

831 the Class I feature representation maps. This data is organized into a single-cell information

832 table, with cells listed in rows and marker expression levels in columns. Finally, unsupervised  
833 clustering algorithms utilize this single-cell information data to identify distinct cell types. (B)  
834 tSNE representation of the marker expression data of about 160k cells from the ovarian cancer  
835 tissue of 83 patients. Cell types were identified by clustering (represented in different colors). (C)  
836 Average marker expression per cluster is shown for the identified cell types, with colors  
837 indicating their corresponding cluster in the *tSNE* representation.



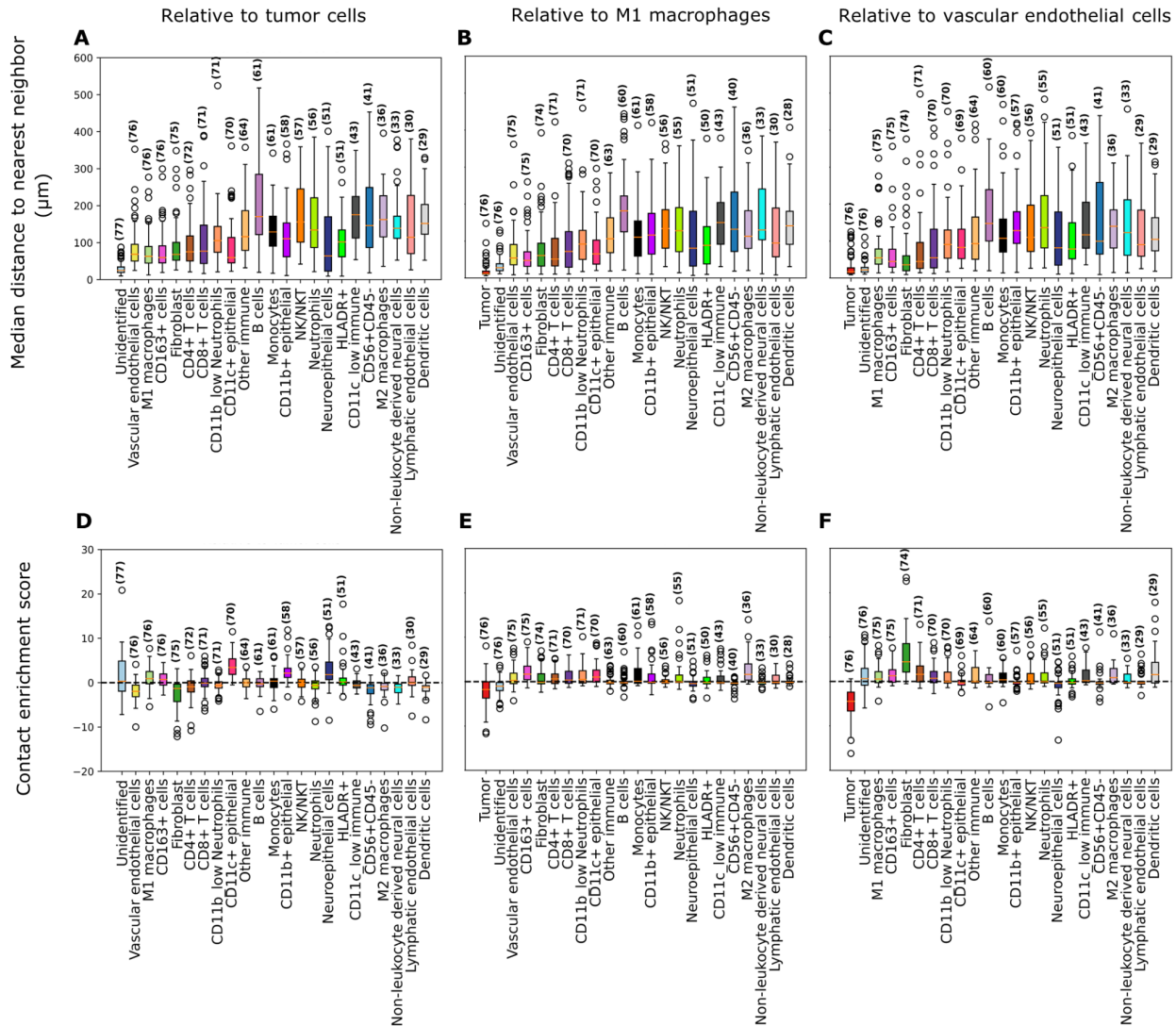
838

839 **Fig 2. TIME composition across samples.** (A) Cell type counts across all 83 samples. (B) Cell

840 type percentages summarized across the 83 original samples, sorted by decreasing tumor cell

841 percentage. (C) Counts of the final 77 samples included in the analysis in which each of the cell

842 types were found.



843

844 **Fig 3. Median nearest neighbor distance (spatial) and contact enrichment (network)**

845 **features relative to three focal cell types. (A-C) Median nearest neighbor distance for each**

846 **other cell type to tumor cells, M1 macrophages, or vascular endothelial cells (μm). (D-F) Contact**

847 **enrichment scores relative to tumor cells, M1 macrophages, or vascular endothelial cells for each**

848 **of the other cell types. Positive scores indicate more contacts than expected at random, 0 the**

849 **same number, and negative scores fewer contacts than expected at random. All bar plots show**

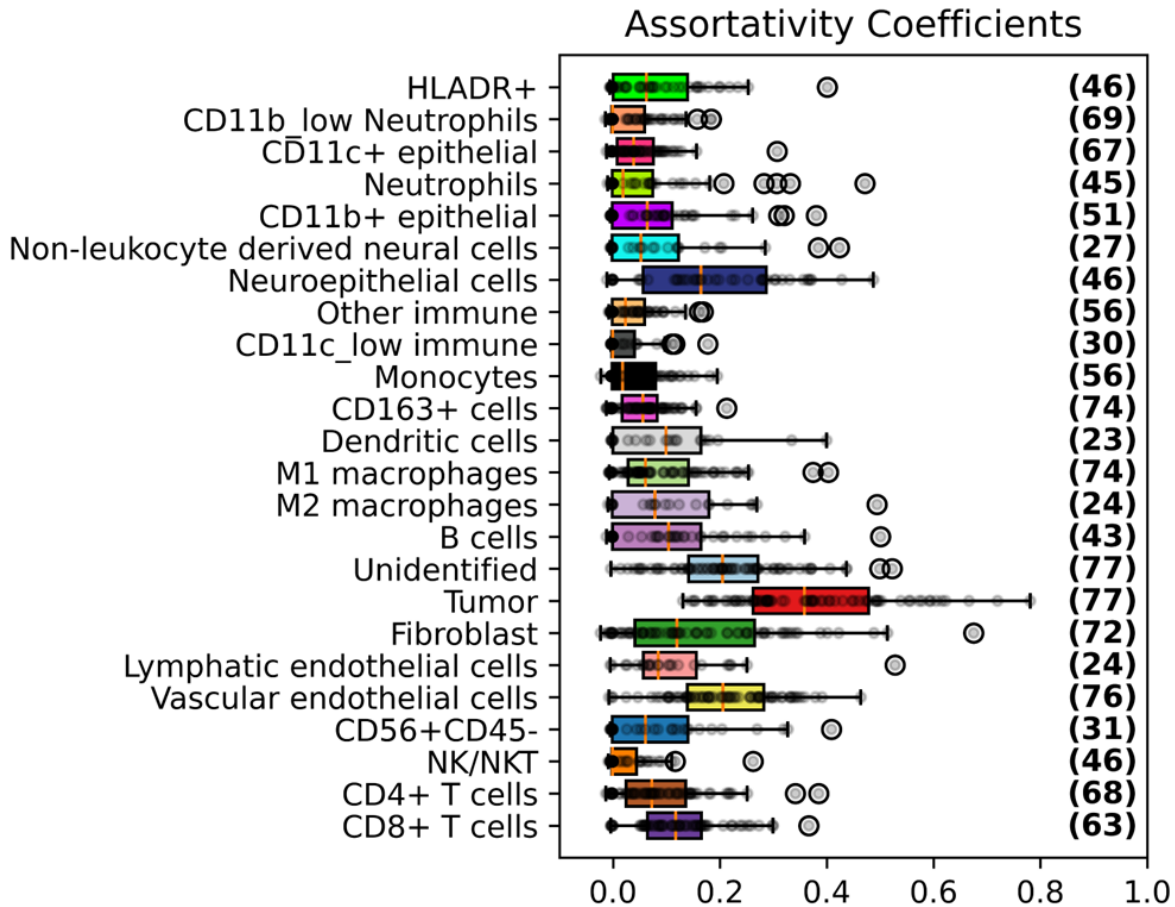
850 **features aggregated across samples in which the relevant cell type is found. Cell types are**

851 **indicated on the x-axis and the number of samples in which this cell type is found is shown in**



852 parentheses. Samples are excluded from the features calculated relative to M1 macrophages and  
853 vascular endothelial cells respectively when samples are missing the respective focal cell type.  
854 In all subplots cell types are ordered based on how commonly they were found across samples in  
855 descending order.

856



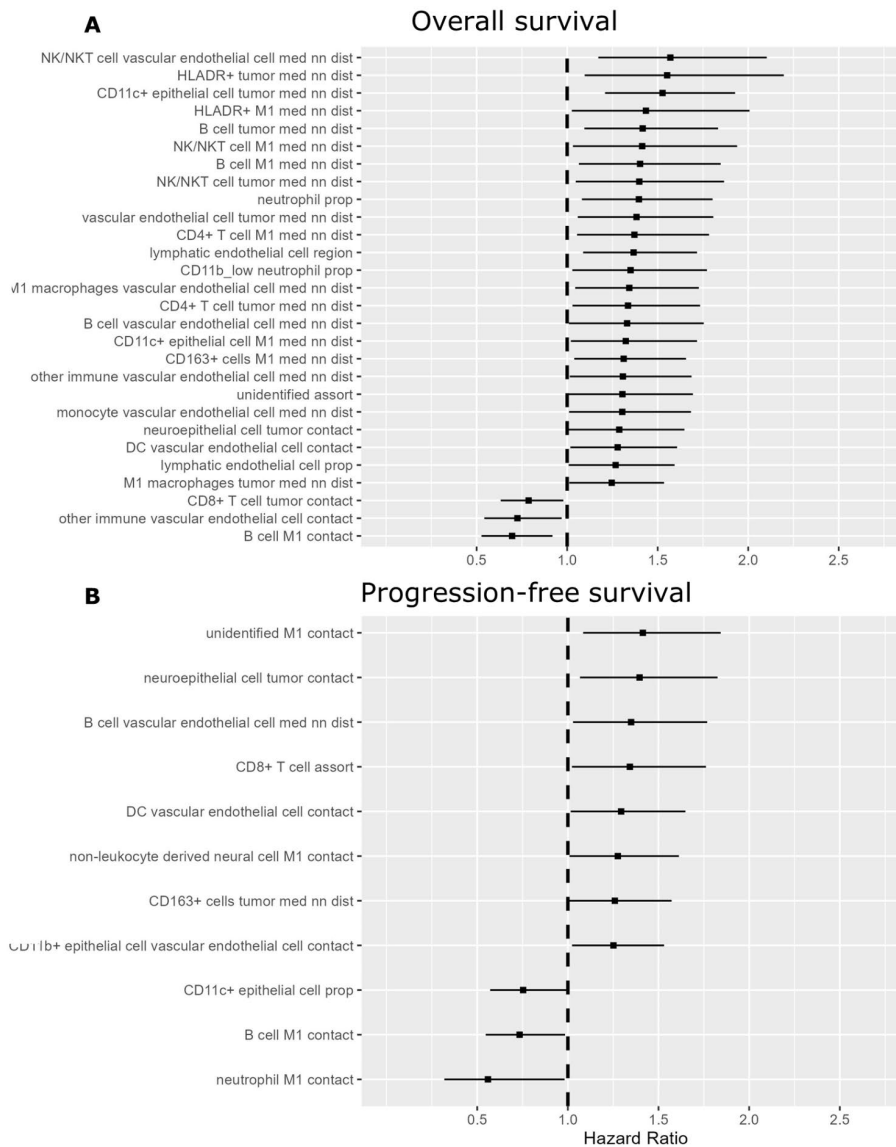
857

858 **Fig 4. Assortativity coefficient (network) features.** Assortativity coefficients for each cell type

859 indicating their tendency to cluster with cells of the same type rather than cells of a different

860 type, aggregated across samples including that cell type (the number of which is indicated in

861 parentheses).



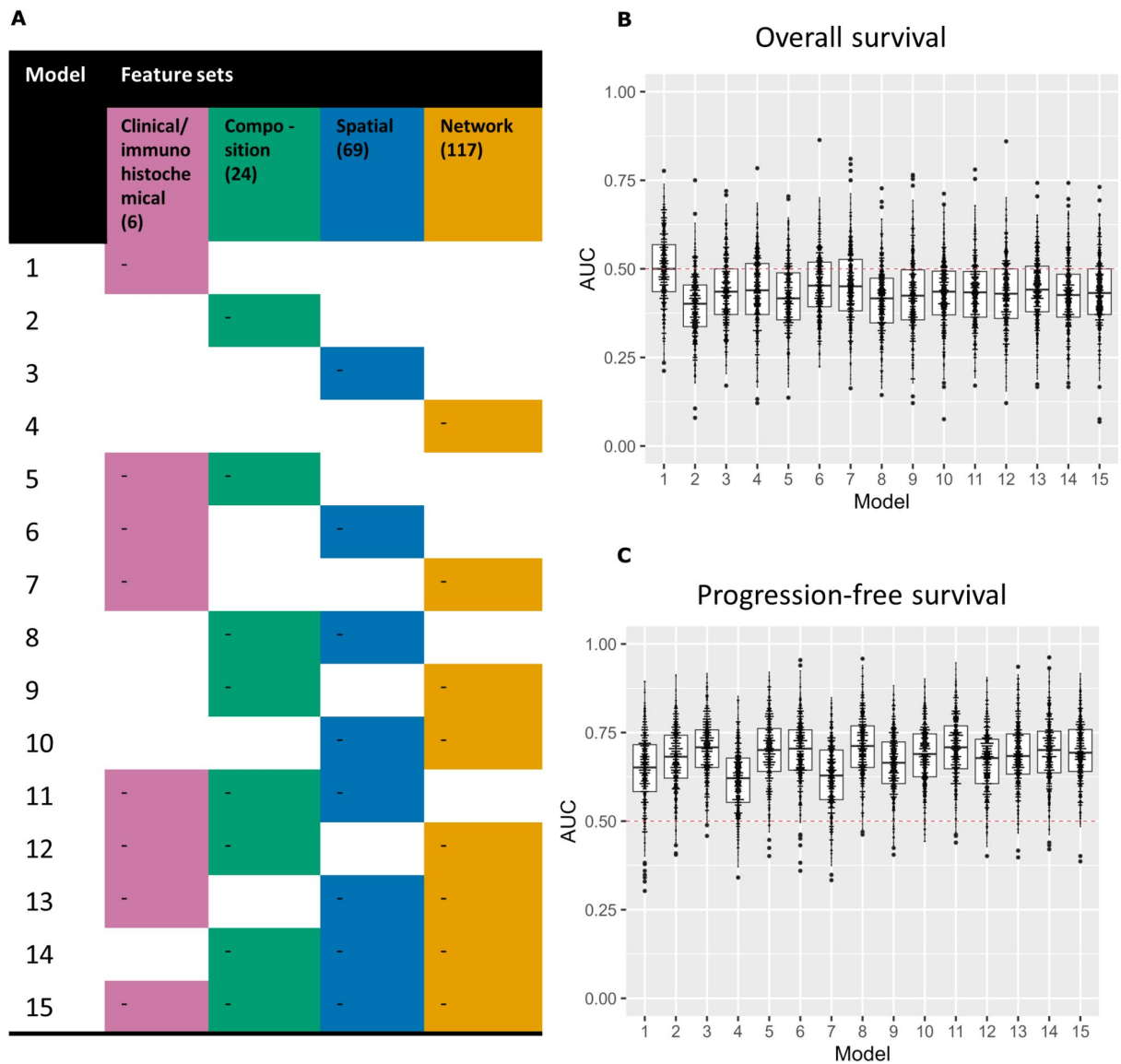
862

863 **Fig 5. Univariate Cox regression results.** Covariates found to be significant in Univariate Cox

864 regressions for (A) OS and (B) PFS outcomes. Covariates are listed in descending order by

865 hazard ratio. Hazard ratios are displayed with 95% confidence intervals, and a hazard ratio of 1 is

866 indicated with a dashed line.



867

868 **Fig 6. Random forest predictive performance results.** (A) 15 models were trained and

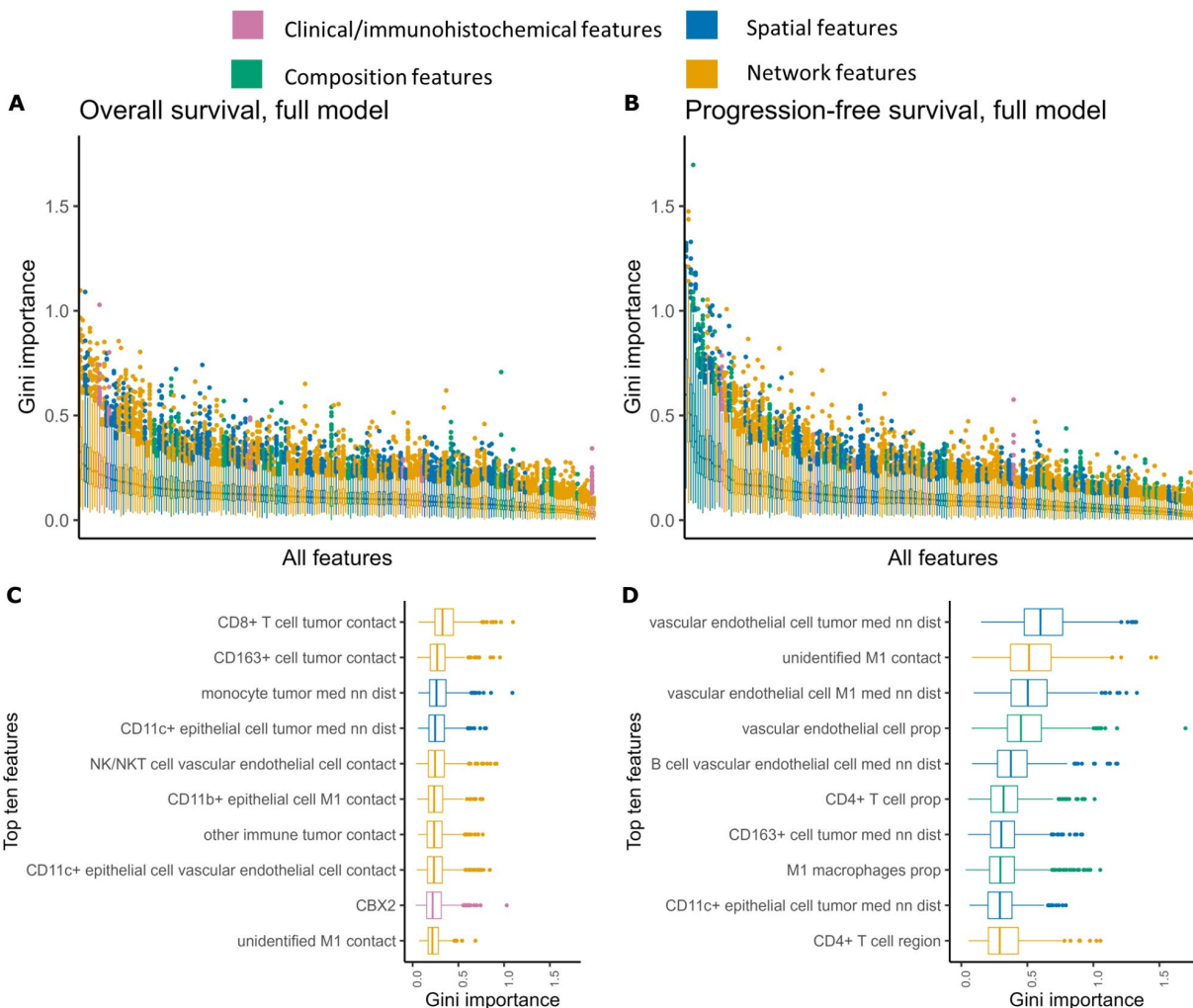
869 evaluated with different combinations of four feature categories, as shown here. Predictive

870 performance results, based on the AUC statistic are displayed for the 15 models summarized

871 across 500 iterations of training and evaluation for (B) OS and (C) PFS outcomes. A red dashed

872 line is displayed at an AUC value of 0.5, which represents the cut-off above which the model

873 performs better than a random guess.



874  
875 **Fig 7. Aggregate feature importance results.** Gini importance scores, aggregated across 500  
876 random forest training runs for the model including all features, sorted by median importance  
877 score and colored by feature type for (A) OS and (B) PFS outcomes. (C-D) Top ten features by  
878 median importance score for each outcome across 500 random forest training runs, colored by  
879 feature type.